

Photon total angular momentum manipulation: Supplementary Material

Lang Li^{1,2,3}, Yingchi Guo^{1,2,3}, Zhichao Zhang^{1,2,3}, Zijun Shang^{1,2,3}, Chen Li^{1,2,3}, Jiaqi Wang^{1,2,3}, Liliang Gao^{1,2,3},

Lan Hai^{1,2,3}, Chunqing Gao^{1,2,3} and Shiyao Fu^{1,2,3,*}

¹ School of Optics and Photonics, Beijing Institute of Technology, Beijing 100081, China

² Key Laboratory of Photoelectronic Imaging Technology and System, Ministry of Education of the People's Republic of China, Beijing 100081, China

³ Key Laboratory of Information Photonics Technology, Ministry of Industry and Information Technology of the People's Republic of China, Beijing 100081, China

* fushiyao@bit.edu.cn

Supplementary Note 1: Opposite phase modulation of TAM separation

As GPOEs introduce opposite phase modulation for orthogonal circular polarizations, the effect not only for the SAM separation, but also for the OAM separation. In order to achieve the TAM separation, the phase modulation of SAM and OAM must be integrated together. Therefore, it is necessary to investigate the negative modulation of ϕ_1 in OAM separation.

The log-polar coordinate transformation term corresponds to the following partial derivative relation:

$$\begin{cases} \frac{\partial \phi_1}{\partial x} = k \frac{u}{f_1} \\ \frac{\partial \phi_1}{\partial y} = k \frac{v}{f_1} \end{cases} \quad (\text{S1})$$

and the partial derivative relation of the opposite phase modulation ϕ_1' can be written as:

$$\begin{cases} \frac{\partial \phi_1'}{\partial x} = -k \frac{u}{f_1} \\ \frac{\partial \phi_1'}{\partial y} = -k \frac{v}{f_1} \end{cases} \quad (\text{S2})$$

When the phase modulation becomes negative, the point (x, y) originally mapped to (u, v) will be mapped to $(-u, -v)$. As for the arc tangent term, the complex coefficients c_q are used to regulate the complex amplitude relations of different diffraction orders³³ and the symmetric orders have the same coefficients. Though they take the opposite values, the relative strength relationship between these diffraction orders remains unchanged. In other words, the opposite fan-out modulation will get the same effect, namely, the original is mapped into a set of rectangular shapes, but the position is symmetric with the original position about the origin.

After corrector modulation, the Fourier transformation of L_2 converts the beam from rectangular shape into strip pattern (sinc function). In the separation plane (ξ, η) , the separated

OAM components in η -axis read:

$$U_l(\eta) = \frac{2\pi a}{\sqrt{N}} \text{sinc}\left(\frac{\eta - \Delta l}{\Delta / N}\right) \quad (\text{S3})$$

where Δ is the half-width of the main flap of the cardinal *sinc* function and l is the topological charge. As for the negative phase modulation cases, it turns to:

$$U_l'(\eta) = \frac{2\pi a}{\sqrt{N}} \text{sinc}\left(\frac{\eta' + \Delta l}{\Delta / N}\right) \quad (\text{S4})$$

Eq. (S4) indicates that, for the OAM separation, when the phase modulation of unwrapper being opposite, both of the adjacent mode spacing and the mode width are unchanged, and only the mode layout changes. Since the opposite circular polarization has an opposite linearly gradient phase, the separated modes from positive and negative modulation are centrosymmetric at the separation plane.

Fig. S1 gives the simulation results when single TAM modes $|\psi_1\rangle = |L\rangle|+4\rangle$ and $|\psi_2\rangle = |R\rangle|+4\rangle$ are incident, which agree well with above analysis.

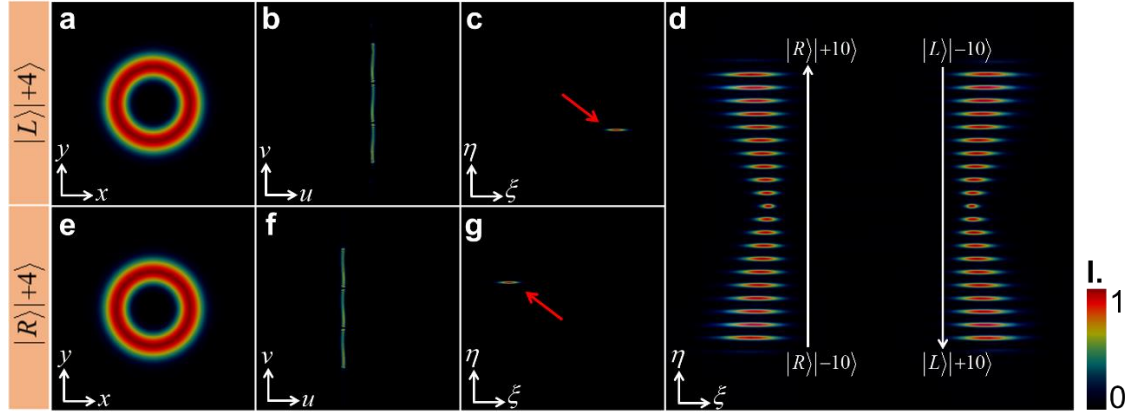


Fig. S1 Simulated intensities distributions of single TAM states on input plane **(a)** **(e)**, rear focal plane of lens L_1 **(b)** **(f)**, and separation plane **(c)** **(g)**. Simulated intensities distribution of all 42 single TAM states in separation plane **(d)**.

Supplementary Note 2: TAM reverser design

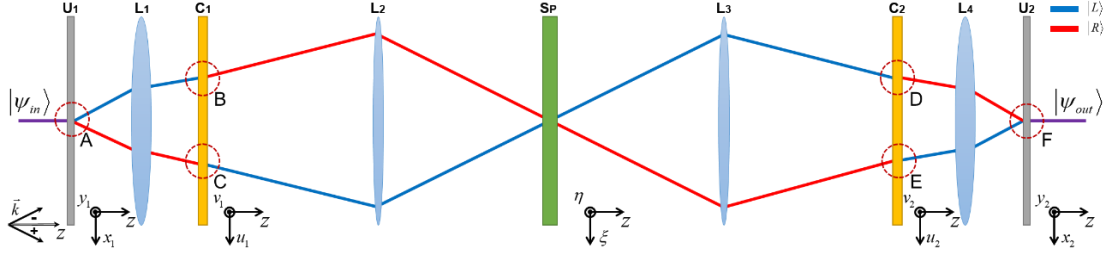


Fig. S2 Principles of TAM mode recovers through the proposed TAM reverser. U_1 , unwrapper; L_{1-4} , lenses; C_1 , corrector; Sp , separation (filter) plane; C_2 , anti-corrector; U_2 , anti-unwrapper.

The TAM reverser should transform the separated states back into the incident form, the structure of which is quasi-symmetric with the TAM separator unit. It's worth analyzing the status of $|\psi\rangle$ during its propagation, given in Fig. S2. Since the OAM modes have a symmetric distribution in vertical axis with opposite phase modulation, and the vertical symmetry of phase distributions ϕ_1 , ϕ_2 , there are no challenge in OAM modes reverse. Considering an incident TAM mode $|\psi_{in}\rangle = |L\rangle|l\rangle$, a complete theoretical analysis is given below.

At first, the input mode is modulated by unwrapper U_1 at region A, and the propagation from A to C is expressed as:

$$M_{L_1} M_{U_1} |\psi_{in}\rangle = |R\rangle|l\rangle_{+\delta_1/f_1} \quad (S5)$$

where M_{U_1} and M_{L_1} are the transformation of U_1 and L_1 , separately. $|R\rangle|l\rangle_{+\delta_1/f_1}$ is the mode irradiated onto (u_1, v_1) plane. $+\delta_1/f_1$ denotes the angular distance of propagation vector and f_1 is the focal length of L_1 .

Subsequently, the mode is modulated by corrector C_1 at region C, described as:

$$M_{C_1} |R\rangle|l\rangle_{+\delta_1/f_1} = |L\rangle|l\rangle_{+\delta_1/f_1 + \delta_2/f_2} \quad (S6)$$

$M_{C_1} = -2\alpha_2$ is the transformation of right half part of C_1 and f_2 is the focal length of L_2 . The mode will propagate further away from the z -axis after the modulation of C_1 , then it passes through a $4-f$ system consisting of L_2 and L_3 . Such propagation from region C to D is expressed as:

$$M_{L_2 L_3} |L\rangle|l\rangle_{+\delta_1/f_1 + \delta_2/f_2} = |L\rangle|l\rangle_{-\delta_1/f_1 - \delta_2/f_2} \quad (S7)$$

where $M_{L_2 L_3}$ is the transformation of the $4-f$ system. Since the propagation vector of $|L\rangle|l\rangle$ is reversed, the modulation of C_2 at region D should take the following form:

$$M_{C_2} |L\rangle|l\rangle_{-\delta_1/f_1 - \delta_2/f_2} = |R\rangle|l\rangle_{-\delta_1/f_1} \quad (S8)$$

To achieve the reversal, the phase modulation at region C and D should be opposite. If C_2 has the same main-axis orientation distribution as C_1 , transformation $M_{C_2} = 2\alpha_2$ seems to be unquestionable. Unfortunately, due to the asymmetric distribution of C_1 in u -axis, the reversal modulation at region D is identical to region C. Moreover, a linear gradient phase modulation $+\delta_2 u / \lambda f_2$ should be introduced by C_2 , simultaneously. Overall, the main-axis orientation distribution of C_2 must be designed as $\alpha_2(u_2, v_2) = \alpha_1(-u_1, v_1)$, namely, C_2 and C_1 are symmetric about the v -axis.

Lastly, L_4 and U_2 are applied to fulfil the final transformation:

$$M_{U_2} M_{L_4} |R\rangle|l\rangle_{-\delta_1/f_1} = |L\rangle|l\rangle_0 \quad (\text{S9})$$

where M_{U_2} and M_{L_4} are the transformation of U_2 and L_4 , separately. As the mode passes through L_4 , it is located at region F, center of the element. Since the input of U_2 is right circularly polarized, M_{U_2} should be $-2\alpha_1$. In other words, U_2 has the same main-axis arrangement as U_1 .

In general, we give the theoretical transformation detail of TAM manipulator with an incident state $|L\rangle|l\rangle$ and complete the design of TAM reverser, while the state $|R\rangle|l\rangle$ can be analyzed in the same manner.

Supplementary Note 3: TAM mode transformation in TAM manipulator

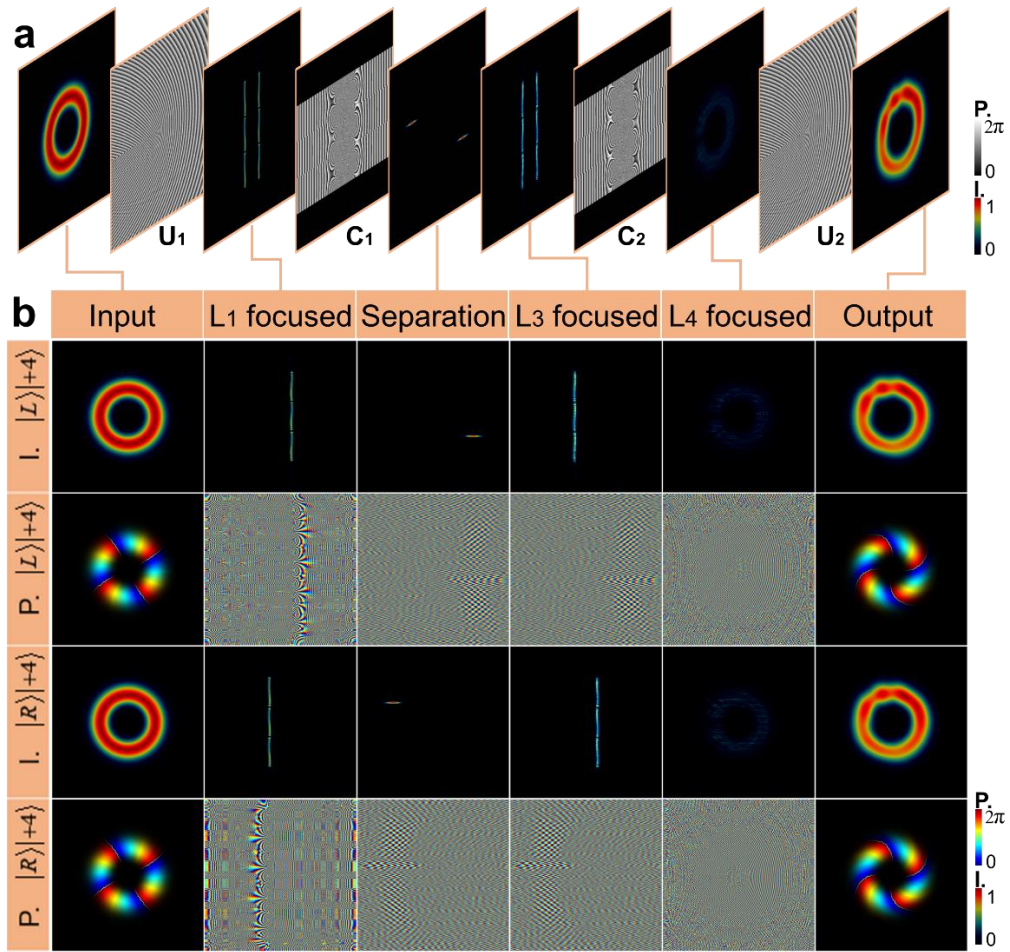


Fig. S3 Transformation process of TAM manipulator for TAM mode $|\psi\rangle = (|L\rangle + |R\rangle)|+4\rangle$. (a) the propagation detail where $L_1 \sim L_4$ are omitted. (b) intensities and phases distributions of various observing planes of two single TAM components $|L\rangle|+4\rangle$ and $|R\rangle|+4\rangle$.

Supplementary Note 4: Simulated and experimental evaluation for TAM separation

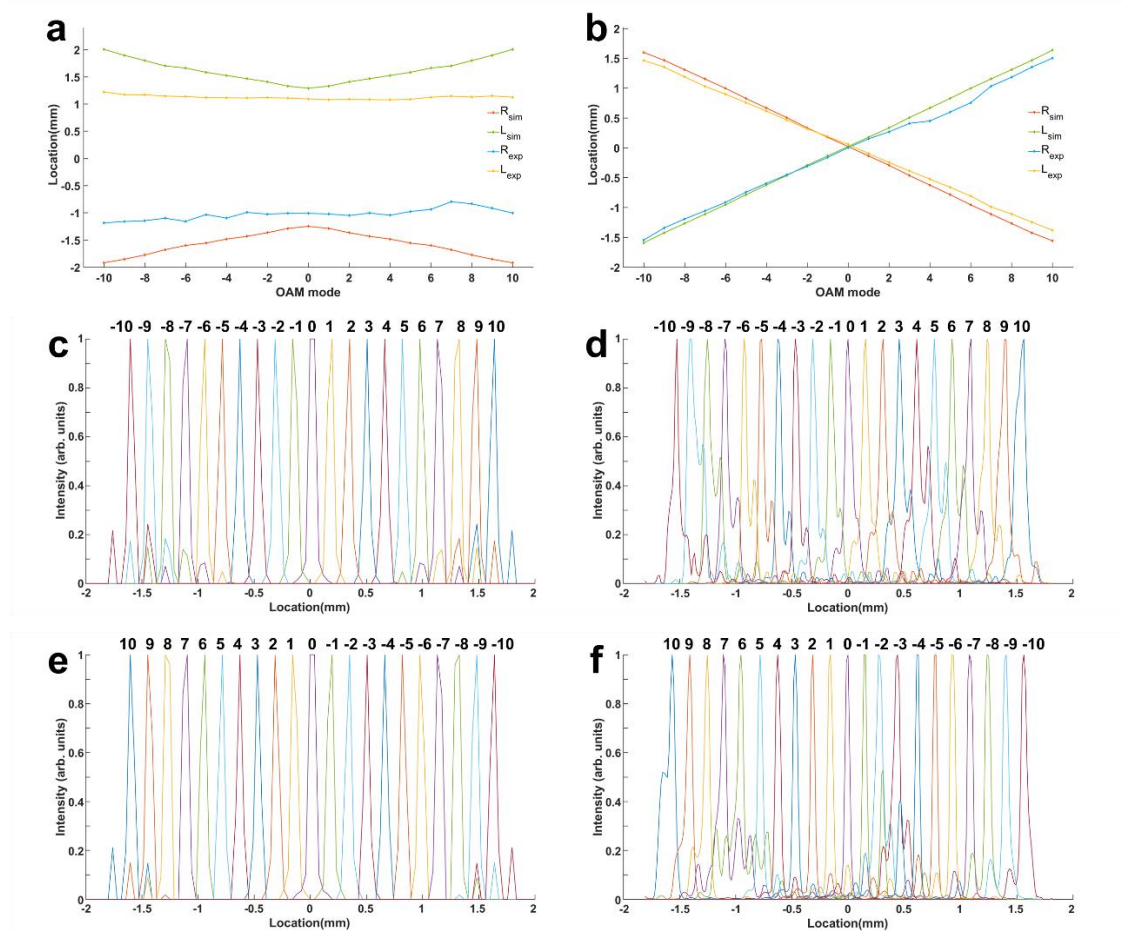


Fig. S4 The simulated and experimental evaluation for TAM separation. **(a)** The maximum intensity locations of TAM states along η axis, including simulation (sim) and experiment (exp) for left and right circular polarizations (L and R). **(b)** The maximum intensity locations of TAM states along ξ axis, including simulation (sim) and experiment (exp) for left and right circular polarizations (L and R). **(c)** The simulated relative intensity along ξ axis for left circular polarizations. **(d)** The experimental relative intensity along ξ axis for left circular polarizations. **(e)** The simulated relative intensity along ξ axis for right circular polarizations. **(f)** The experimental relative intensity along ξ axis for right circular polarizations. The eigen value of OAM mode are labeled on **(c-f)**.

These plots shown in Fig. S4 are obtained from the simulated and experimental patterns of TAM separation given in Fig. S6-17. With the fabricating error of GPOEs, there exists imperfect phase modulation. To get better experimental separation performance, the corrector (C_1) is located slightly away from the rear focal plane of the first lens (L_1), which only brings about the difference between the simulated and experimental in Fig. S4a. Fig. S4b illustrate that the experimental location of each TAM state along ξ axis is basically consistent with the simulation, while there are some deviations from three states, $|R\rangle|l\rangle$ ($l=4,5,6$), which might be caused by the slight misalignment between the unwrapper (U_1) and corrector (C_1).

Integrating the power in η axis could generate Fig. S4c-f, where the experimental results is favorable with the simulation. As Eq. S3 and Eq. S4 contain a sinc function, side-lobe crosstalk is inevitable for this log-polar transformation-based separation. To quantitatively evaluate the impact of this crosstalk, a concept like side mode suppression ratio, defined as the ratio of the intensity between the maximum and secondary peaks in Fig. S4c-f for each mode, could be applied. For the simulation, this indicator is greater than 20 dB when the eigen value l of OAM mode meets $|l| \leq 8$, while the average of it goes to 16.40dB in other states. Due to the imperfect phase modulation and experimental misalignment mentioned above, the indicator decreases to 15.67dB in experiment, which can be closer to the simulation with the improvement of fabrication techniques and the integration of the unwrapper and corrector.

Supplementary Note 5: Experimental details

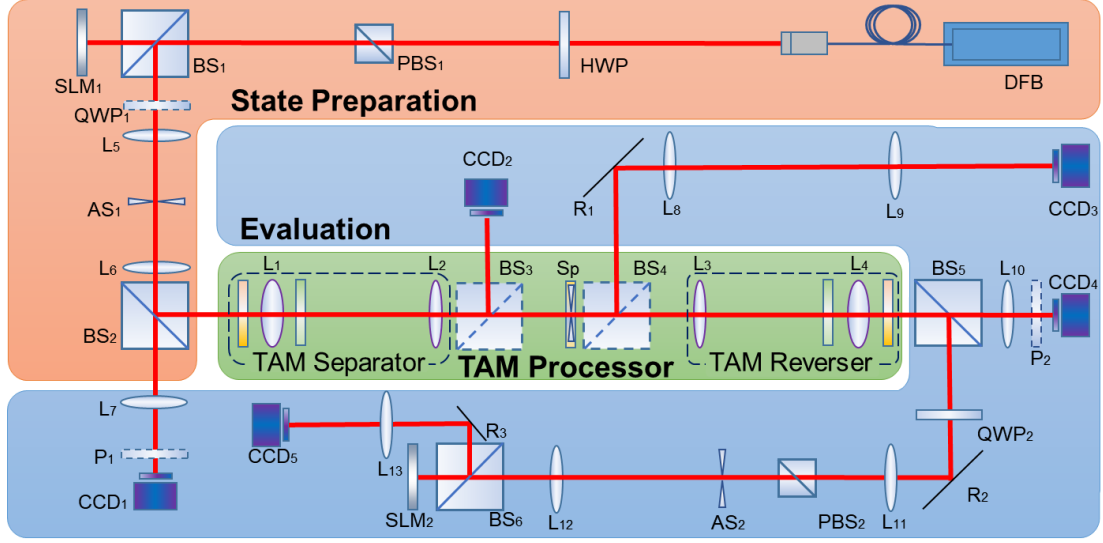


Fig. S5 The experimental setup. DFB, distributed feedback laser diode; SMF, single mode fiber; COL, collimator; HWP, half wave plate; PBS₁ & PBS₂, polarized beam splitter; BS₁ ~ BS₆, beam splitter; SLM₁ & SLM₂, liquid-crystal spatial light modulator; QWP₁ & QWP₂, quarter wave plate; L₁ ~ L₁₃, plano-convex lenses, the focal length of L₂ & L₄ ~ L₁₃ are 200mm and the focal length of L₁ & L₃ are 50mm; AS₁ & AS₂, aperture stop; TAM Separator, Sp and TAM Reverser, the units of TAM manipulator; R₁ ~ R₃, reflector; P₁ & P₂, polarizer; CCD₁ ~ CCD₅, infrared CCD camera.

We evaluated the system through the setup shown in Fig. S4. For the state preparation section, the 1617nm fundamental mode Gaussian beam is generated and coupled into free space from a collimator (COL). Then the beam was converted into horizontal linear polarization, by passing through a half wave plate (HWP) and a polarized beam splitter (PBS₁). Next, the TAM beam was generated by encoding special designed holograms on a spatial light modulator (SLM₁). Finally, the generated beam was relayed to the first plane of TAM manipulator through the 4-*f* system consisting of two plano-convex lenses (L₅ & L₆) with an aperture stop (AS₁). Moreover, inserting a quarter wave plate (QWP₁) in the path and rotating could transform the incident beam from horizontal linear polarization into either of the two orthogonal circular polarizations.

The setup of TAM manipulator was consistent with Fig. 1. As for the evaluation section, the intensity distributions of incident beam were captured by an infrared CCD camera (CCD₁) with a plano-convex lens (L₇), and a polarizer (P₁) was inserted when doing the polarization detection. A beam splitter (BS₃) and CCD₂ was placed after the TAM separator for the capture of the intensity distributions of separated beam. Then, a 4-*f* system consisting of two plano-convex lenses (L₈ & L₉), along with a beam splitter (BS₄) and a reflector (R₁), relayed the filtered patterns on the separation

plane to the infrared CCD camera (CCD₃) for evaluation. The output pattern of TAM manipulator was captured by the infrared CCD camera (CCD₄) together with plano-convex lens (L₁₀). A polarizer (P₂) was inserted when doing the polarization detection.

For the TAM spectrum analysis of output beam, a $4f$ system consisting of two plano-convex lenses (L₁₁ & L₁₂), along with a beam splitter (BS₅) and a reflector (R₂), delivered the output beam to a spatial light modulator (SLM₂), which is encoded by a series of holographic anti-spiral phase plates (HASPPs) for the OAM projection measurement²⁶. Meanwhile, the SAM projection measurement is carried out by a quarter wave plate (QWP₂) together with a polarized beam splitter (PBS₂). The projected modes were reflected by beam splitter (BS₆) and reflector (R₃) twice, and then captured by an infrared CCD camera (CCD₅). Finally, the TAM spectrum was obtained.

In the theory of TAM manipulator, focal length of the second and the fourth lens (L₂ & L₄) are originally 400mm, due to the limitation of the length of optical table, the focal length is reduced to 200mm. The effect of modifying this parameter is only to scale down the pattern to half.

Supplementary Note 6: Simulated and experimental results for TAM manipulator

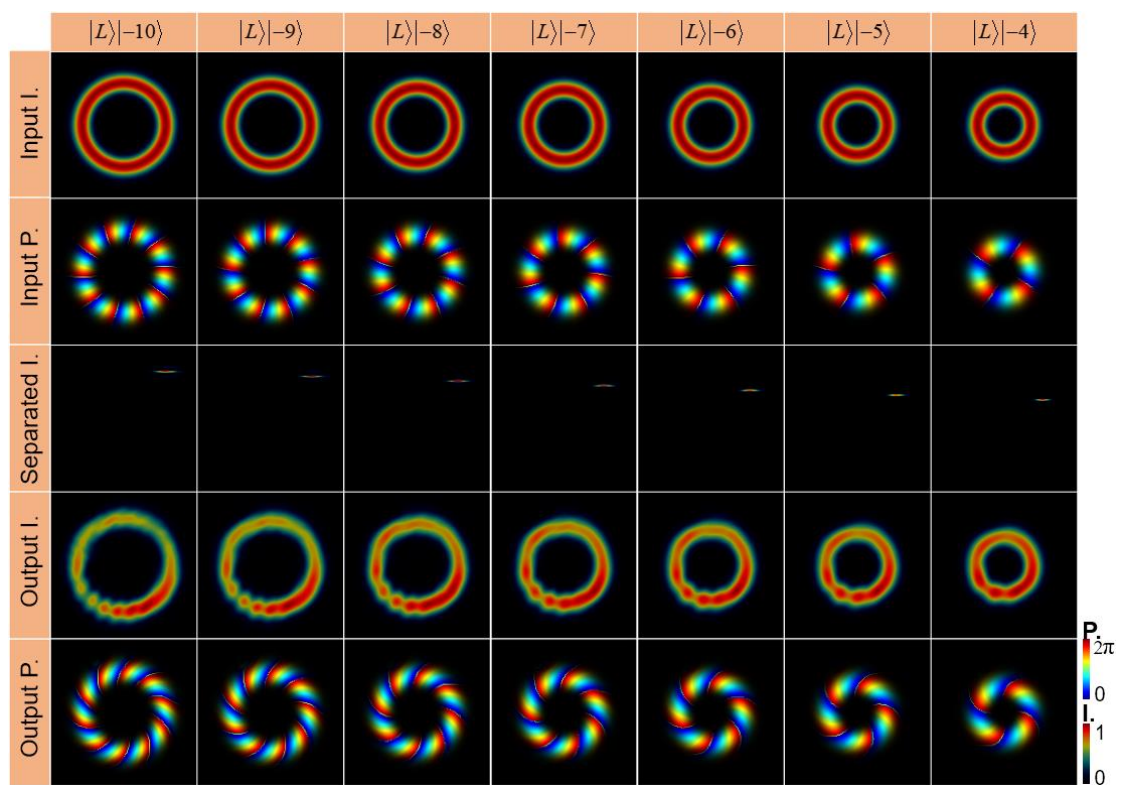


Fig. S6 The simulated results of single TAM states. $|\psi\rangle = |L\rangle|l\rangle$, $l = -10 \sim -4$.

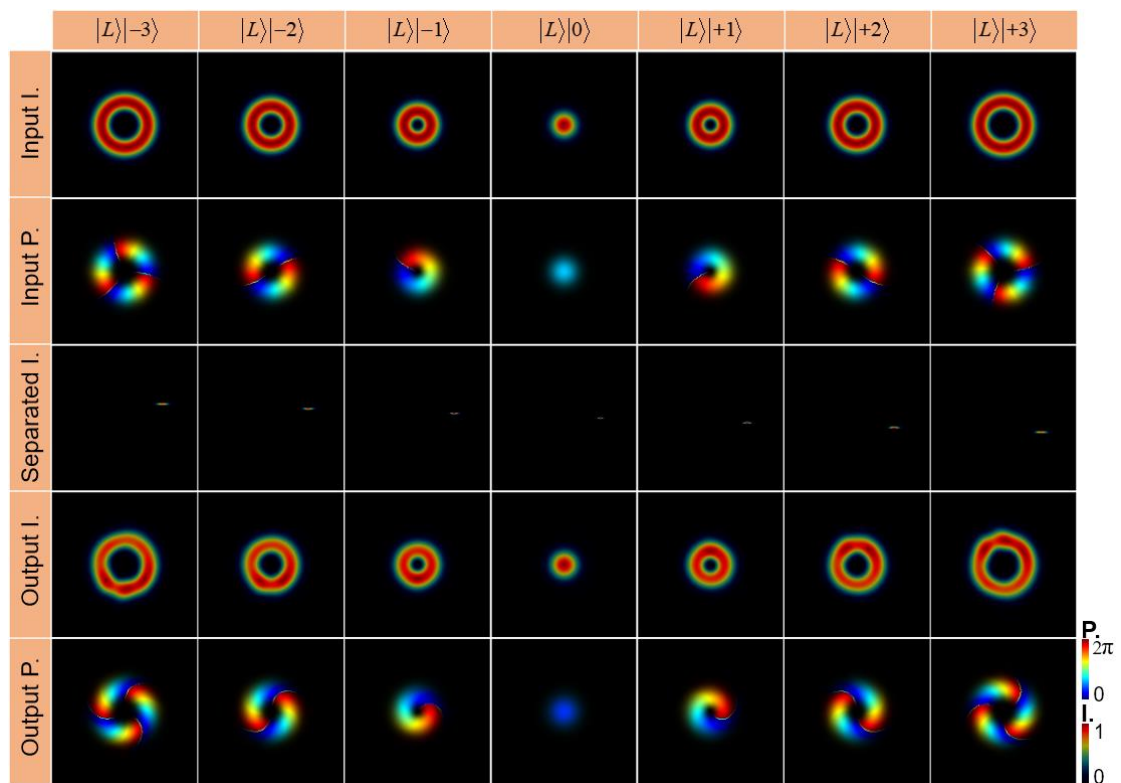


Fig. S7 The simulated results of single TAM states. $|\psi\rangle = |L\rangle|l\rangle$, $l = -3 \sim +3$.

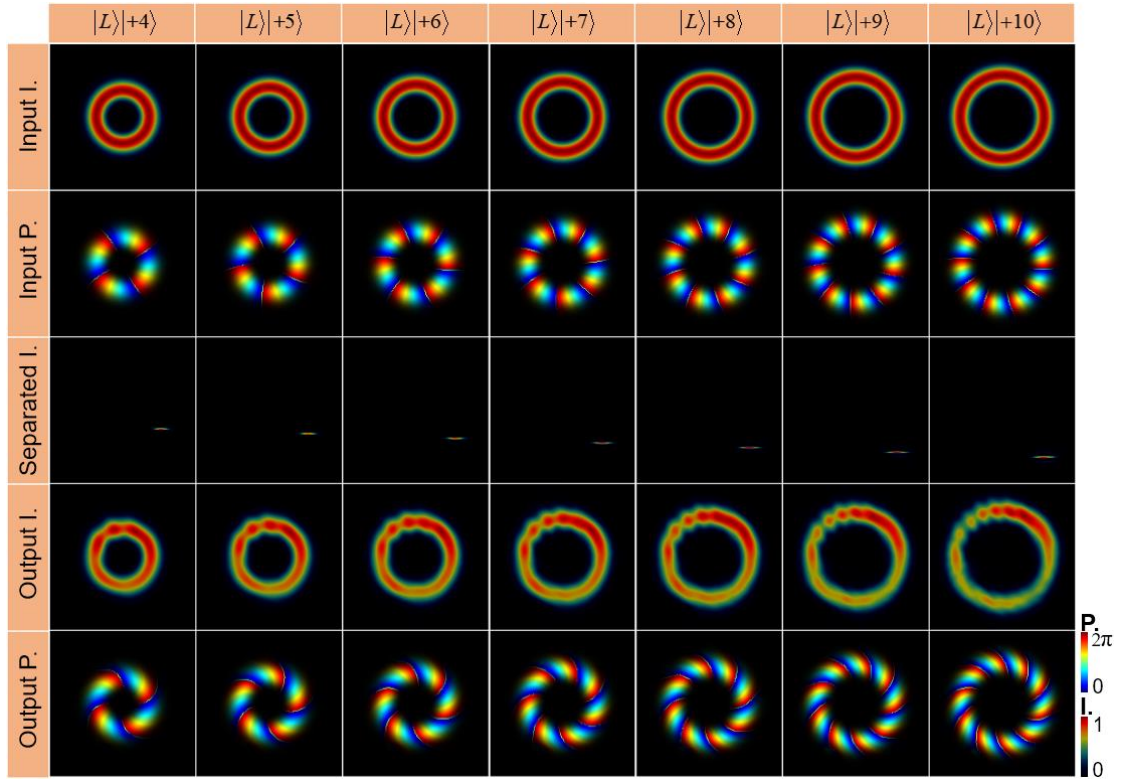


Fig. S8 The simulated results of single TAM states. $|\psi\rangle = |L\rangle|l\rangle$, $l = +4 \sim +10$.

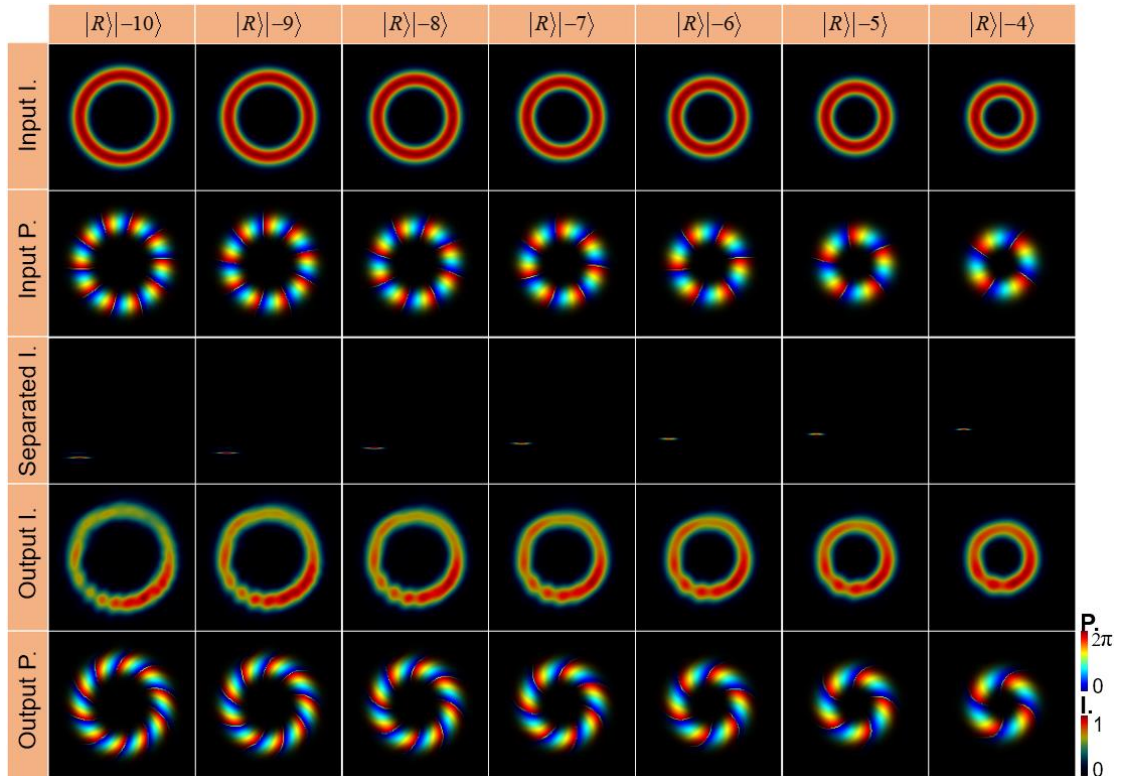


Fig. S9 The simulated results of single TAM states. $|\psi\rangle = |R\rangle|l\rangle$, $l = -10 \sim -4$.

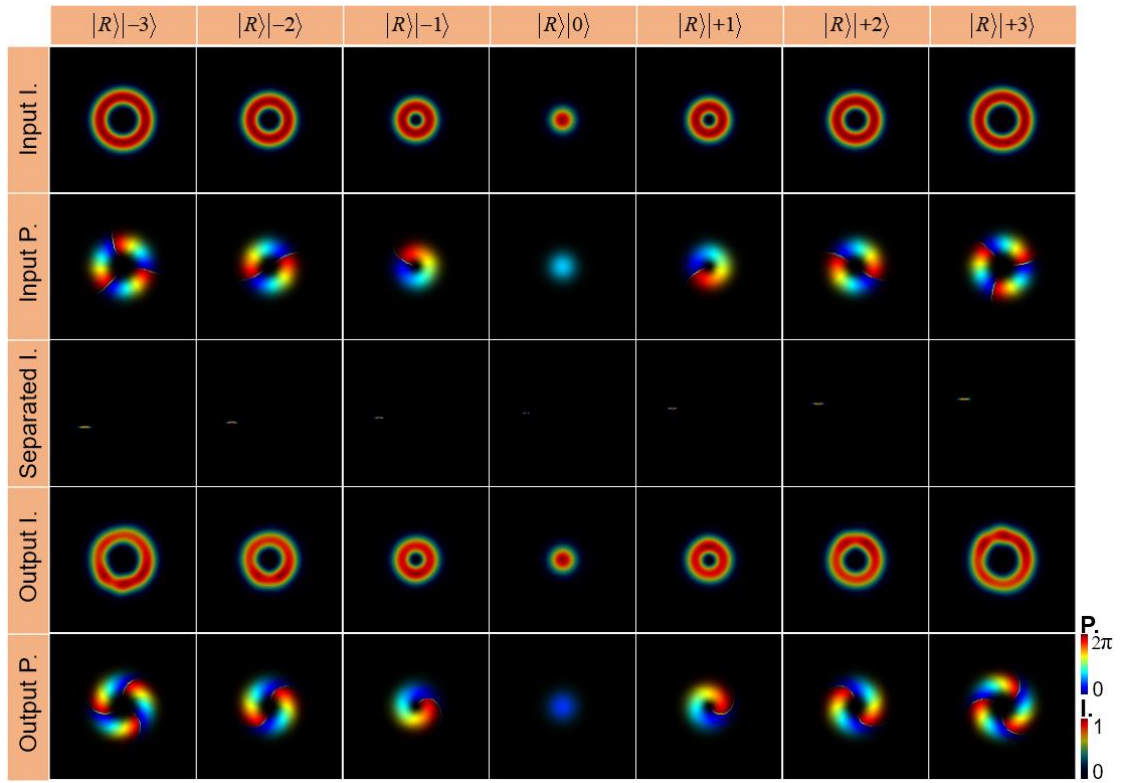


Fig. S10 The simulated results of single TAM states. $|\psi\rangle = |R\rangle|l\rangle$, $l = -3 \sim +3$.

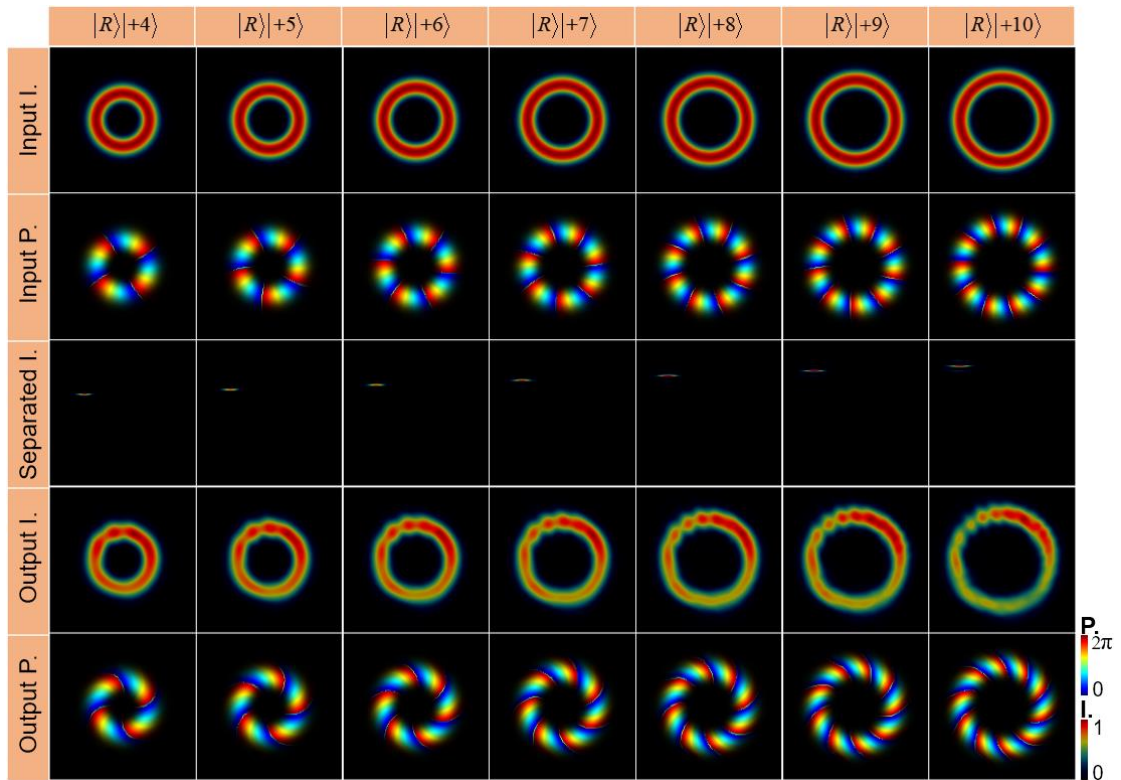


Fig. S11 The simulated results of single TAM states. $|\psi\rangle = |R\rangle|l\rangle$, $l = +3 \sim +10$.

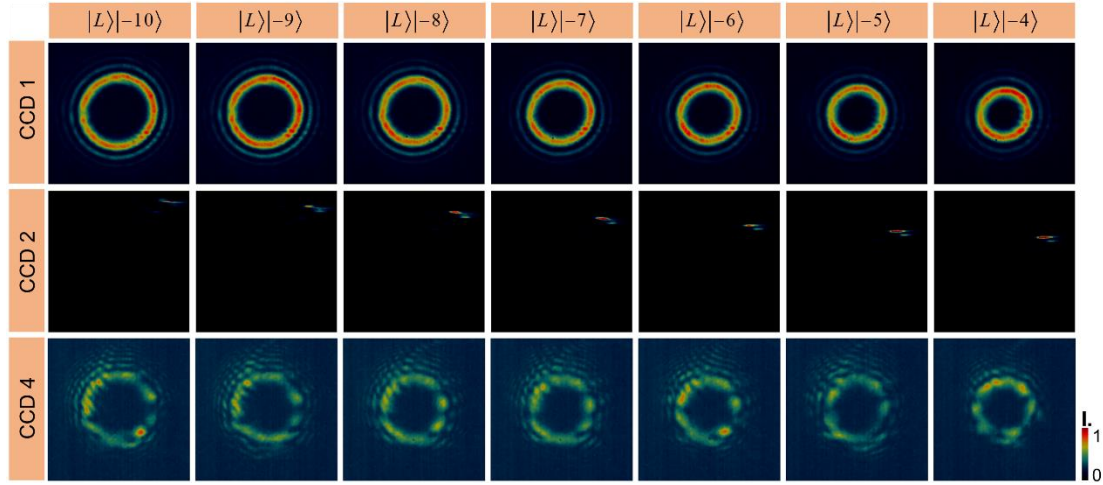


Fig. S12 The experimental intensities distributions of single TAM states at CCD1, CCD2 and CCD4. $|\psi\rangle = |L\rangle|l\rangle$, $l = -10 \sim -4$.

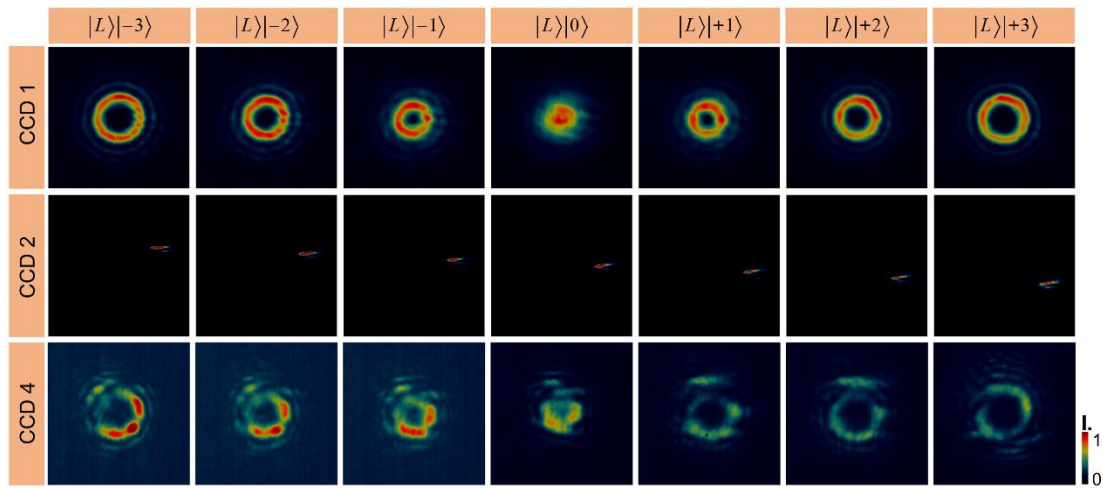


Fig. S13 The experimental intensities distributions of single TAM states at CCD1, CCD2 and CCD4. $|\psi\rangle = |L\rangle|l\rangle$, $l = -3 \sim +3$.

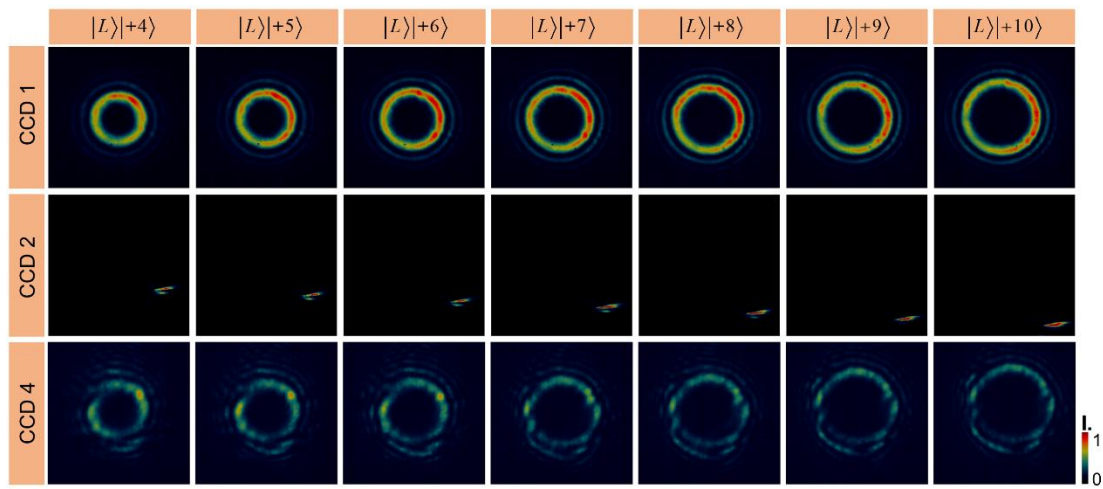


Fig. S14 The experimental intensities distributions of single TAM states at CCD1, CCD2 and CCD4. $|\psi\rangle = |L\rangle|l\rangle$, $l = +4 \sim +10$.

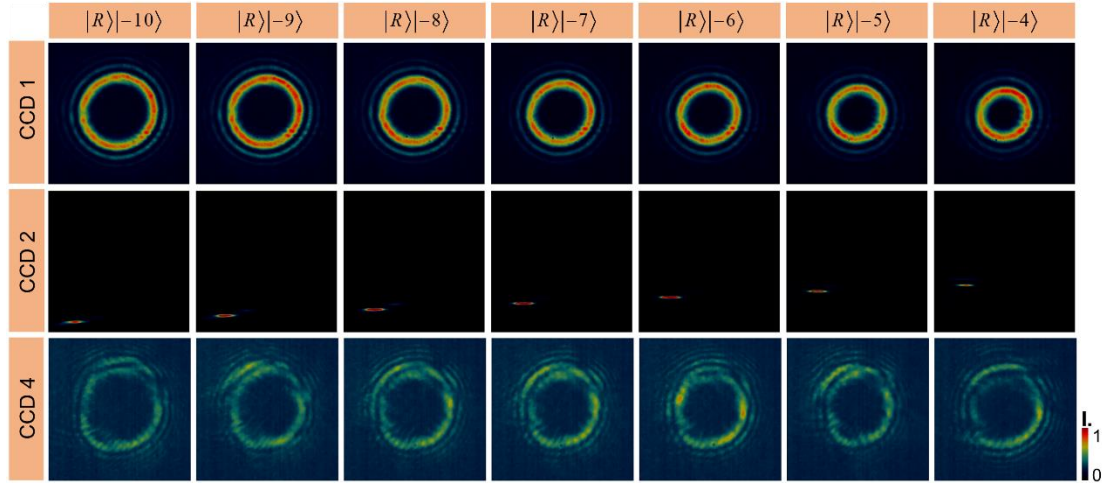


Fig. S15 The experimental intensities distributions of single TAM states at CCD1, CCD2 and CCD4. $|\psi\rangle = |R\rangle|l\rangle$, $l = -10 \sim -4$.

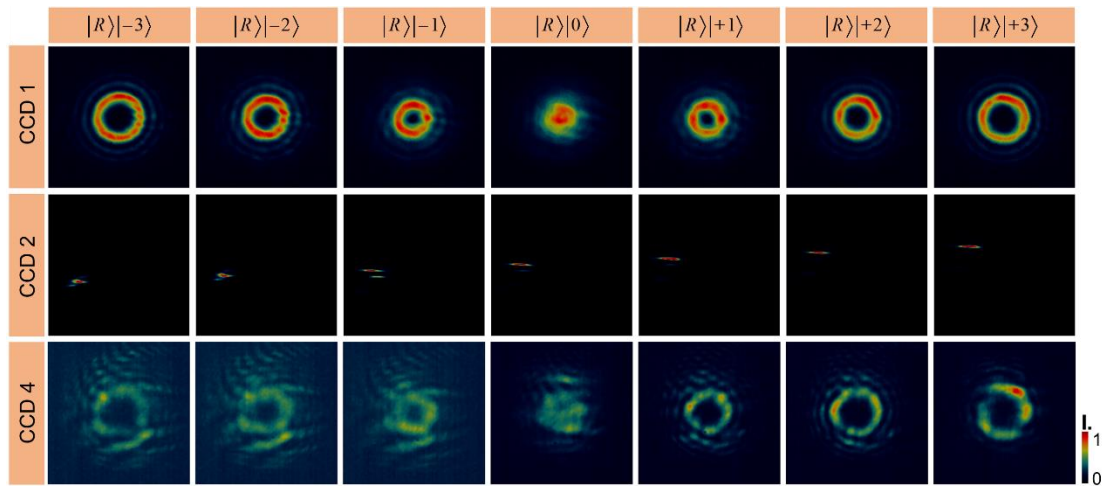


Fig. S16 The experimental intensities distributions of single TAM states at CCD1, CCD2 and CCD4. $|\psi\rangle = |R\rangle|l\rangle$, $l = -3 \sim +3$.

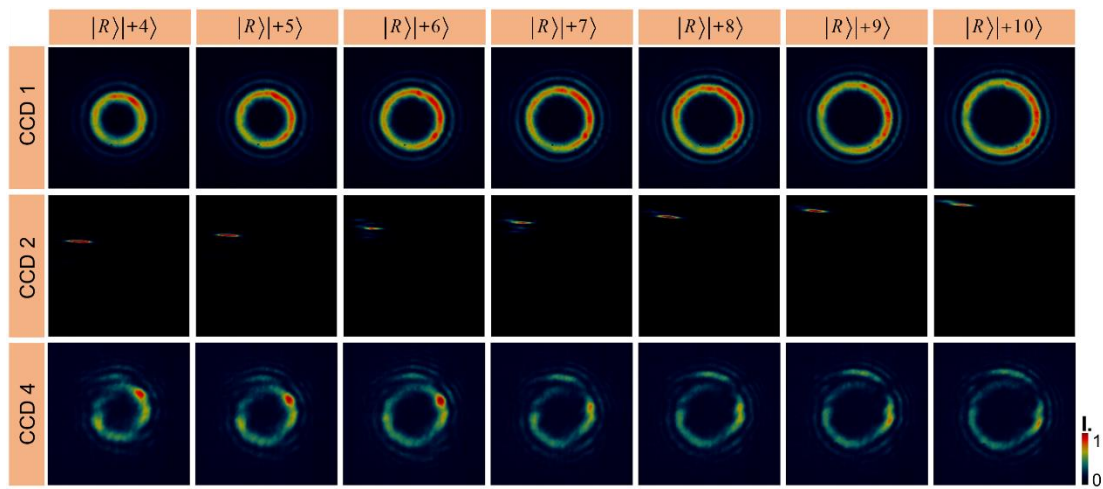


Fig. S17 The experimental intensities distributions of single TAM states at CCD1, CCD2 and CCD4. $|\psi\rangle = |R\rangle|l\rangle$, $l = +4 \sim +10$.

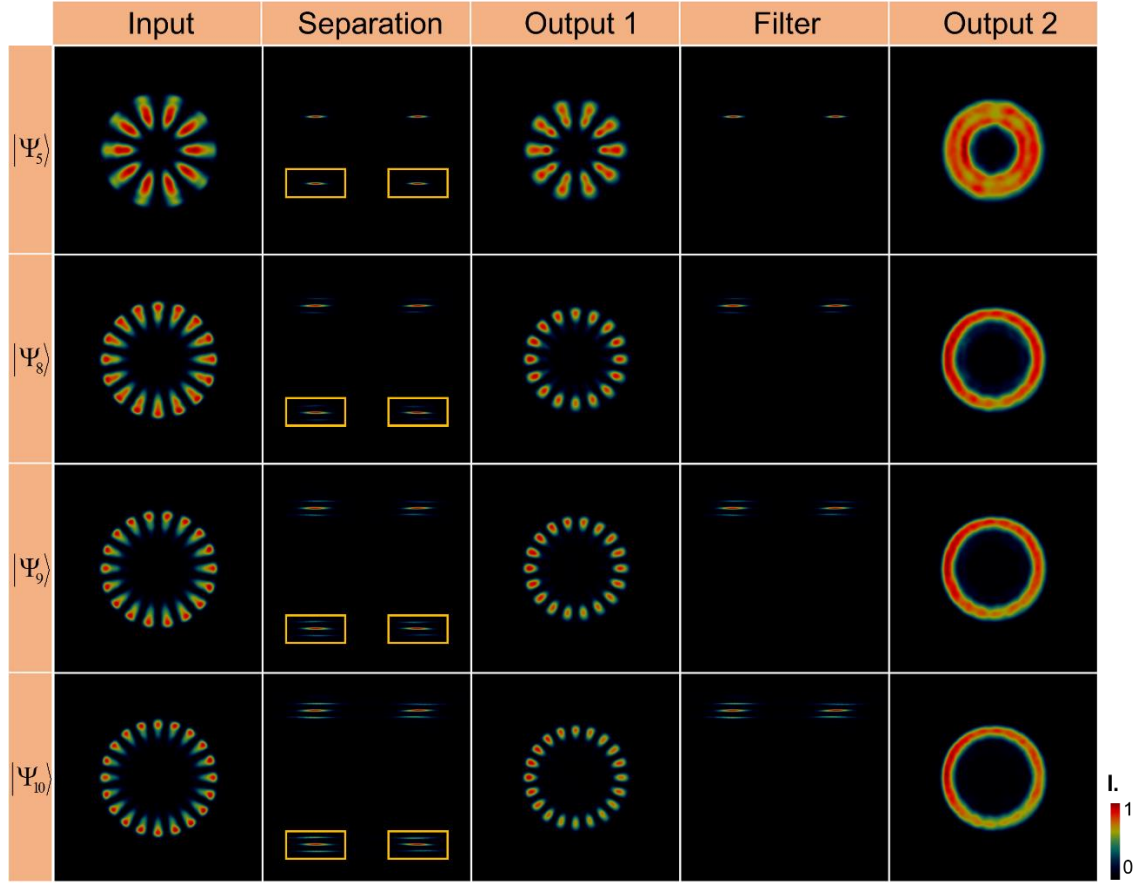


Fig. S18 The simulated results of multi-TAM modes $|\Psi_5\rangle, |\Psi_8\rangle, |\Psi_9\rangle, |\Psi_{10}\rangle$ incident. Input, the intensities distributions of incident modes; Separation, the intensities distributions of separated modes; the boxes, the modes blocked in selective blocking cases; Output 1, the intensities distributions of output in straight through cases; Filter, the intensities distributions of modes after blocking; Output 2, the output intensity distributions in selective blocking cases.

Supplementary Note 7: The insufficient phase modulation

As the limitation of the GPOEs' fabrication is exposed, the intensities distributions of the linear polarized OAM carried beam, denoted as $|\psi\rangle = (|L\rangle + |R\rangle)|l\rangle$, propagating to the rear focal plane of the first lens (L_1) are given in Fig. S19. In experimental cases, there exist three spots vertically laying at the center, which represents the focused linear polarized OAM beam, indicating that the imperfect phase modulations are only evident at lower OAM orders.

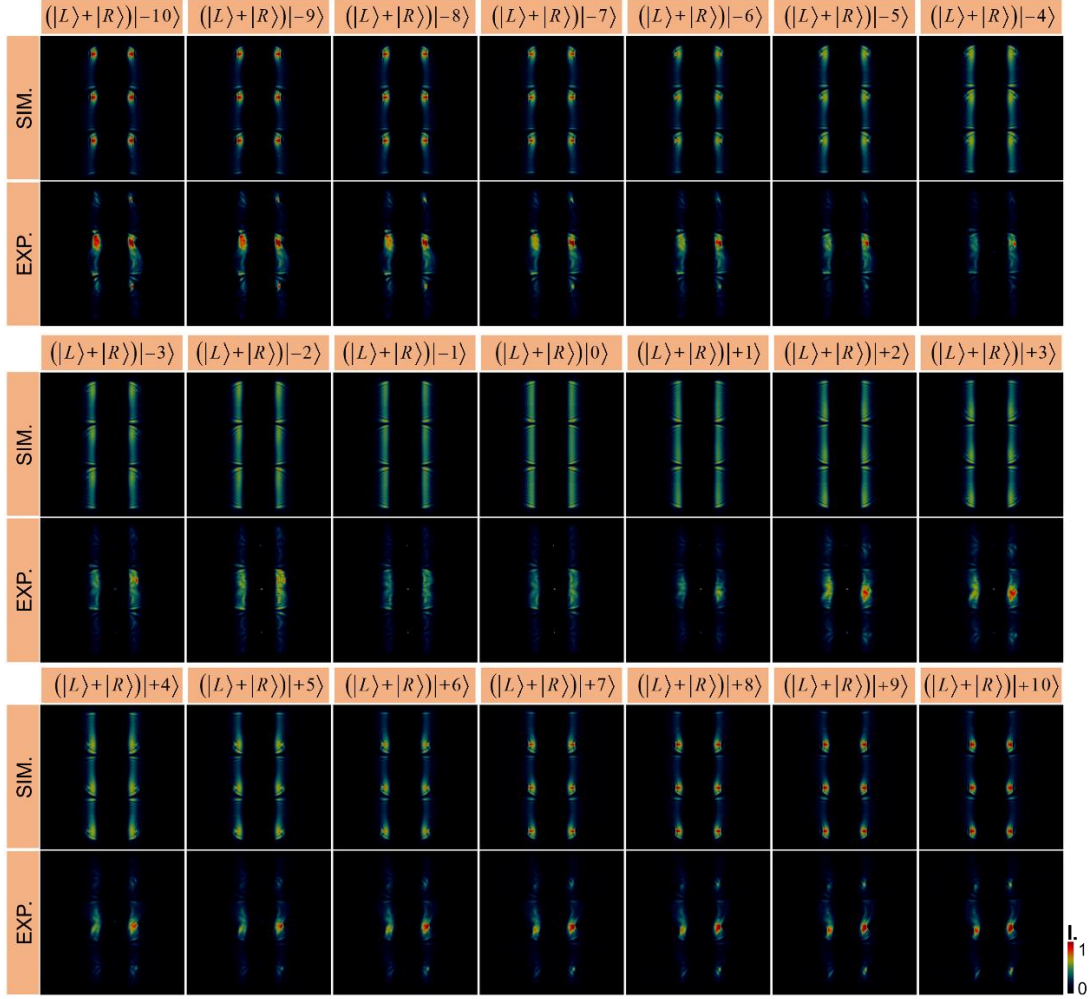


Fig. S19 The simulated and experimental patterns of linear polarized OAM beam at the rear focal plane of the lens L_1 . $|\psi\rangle = (|L\rangle + |R\rangle)|l\rangle$, $l = -10 \sim +10$.